Journal of
BIOPHOTONICS

FULL ARTICLE

Investigating the healing mechanisms of an angiogenesis-promoting topical treatment for diabetic wounds using multimodal microscopy

Joanne Li[1,2] | Andrew J. Bower[1,3] | Zane Arp[1,4] | Eric J. Olson[4] | Claire Holland[4] |
Eric J. Chaney[1] | Marina Marjanovic[1,2] | Paritosh Pande[1] | Aneesh Alex[1,4] |
Stephen A. Boppart[1,2,3,5]*

[1]Beckman Institute for Advanced Science and Technology, University of Illinois at Urbana-Champaign, Urbana, Illinois

[2]Department of Bioengineering, University of Illinois at Urbana-Champaign, Urbana, Illinois

[3]Department of Electrical and Computer Engineering, University of Illinois at Urbana-Champaign, Urbana, Illinois

[4]Discovery Medicine, HF DPU, GlaxoSmithKline, King of Prussia, Pennsylvania

[5]Carle-Illinois College of Medicine, University of Illinois at Urbana-Champaign, Urbana, Illinois

*Correspondence
Stephen A. Boppart, Beckman Institute for Advanced Science and Technology, University of Illinois at Urbana-Champaign, Urbana, IL 61801.
Email: boppart@illinois.edu

Funding information
GlaxoSmithKline

Impaired skin wound healing is a significant comorbid condition of diabetes that is caused by poor microcirculation, among other factors. Studies have shown that angiogenesis, a critical step in the wound healing process in diabetic wounds, can be promoted under hypoxia. In this study, an angiogenesis-promoting topical treatment for diabetic wounds, which promotes angiogenesis by mimicking a hypoxic environment via inhibition of prolyl hydroxylase resulting in elevation or maintenance of hypoxia-inducible factor, was investigated utilizing a custom-built multimodal microscopy system equipped with phase-variance optical coherence tomography (PV-OCT) and fluorescence lifetime imaging microscopy (FLIM). PV-OCT was used to track the regeneration of the microvasculature network, and FLIM was used to assess the in vivo metabolic response of mouse epidermal keratinocytes to the treatment during healing. Results show a significant decrease in the fluorescence lifetime of intracellular reduced nicotinamide adenine dinucleotide, suggesting a hypoxic-like environment in the wounded skin, followed by a quantitative increase in blood vessel density assessed by PV-OCT. Insights gained in these studies could lead to new endpoints for evaluation of the efficacy and healing mechanisms of wound-healing drugs in a setting where delayed healing does not permit available methods for evaluation to take place.
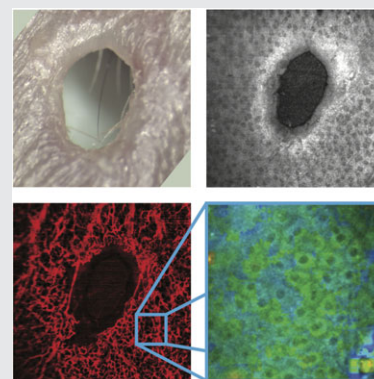
KEYWORDS

diabetes, fluorescence lifetime imaging microscopy, label-free imaging, optical coherence tomography, wound healing

1 | INTRODUCTION

Diabetes affects more than 29 million people in the United States, and this number is projected to double or triple by 2050 [1, 2]. This disease causes many physiological complications, such as diabetic foot ulcers, which contribute to approximately 60% of nontraumatic lower limb amputations among people age 20 years or older [1–3]. Such impaired wound healing in diabetic patients is caused by a variety of physiological abnormalities, one of which is poor microcirculation, which is essential for normal wound healing [4–6]. Due to the importance of blood vessel formation in wound healing, numerous studies have been conducted to investigate the development and efficacy of novel treatments to promote angiogenesis in nonhealing diabetic wounds [7–10]. In this study, the healing mechanisms of a novel topical ointment for diabetic wounds that is capable of promoting angiogenesis by inducing local physiological conditions that mimics hypoxia was investigated.

Angiogenesis has a crucial role in many diseases and physiological responses, including wound healing. In wounds, capillary injury creates a hypoxic environment, triggering the release of essential growth factors and cells to participate in neovasculogenesis and angiogenesis, a process that is often dysfunctional in diabetic wounds [4–6, 11]. The topical treatment being investigated in this study mimics hypoxia via inhibition of prolyl hydroxylase, a key regulator of hypoxia-inducible factor (HIF) [11]. HIF induction in turn results in activation of pathways that mediate the protective and regenerative tissue response to hypoxia, such as angiogenesis, which is relevant in the healing process. Currently, characterizations of wound healing and associated treatments rely heavily on visual inspection, digital photography and ex vivo analysis. To better understand the complex processes of nonhealing diabetic wounds and the healing mechanisms of novel treatments, a technology capable of in vivo, noninvasive, longitudinal tracking of wound healing with cellular-level resolution is imperative.

In recent years, several optical imaging techniques have proven beneficial in observing key biological events, both in vivo and ex vivo, in processes such as wound healing, apoptosis and metabolic changes in the tumor microenvironment, at resolutions unparalleled by conventional techniques [12–17]. In this study, phase-variance optical coherence tomography (PV-OCT) and fluorescence lifetime imaging microscopy (FLIM) were utilized to track the regeneration of the microvasculature network and the change in cellular metabolic activity, respectively, in wounded and healing skin in diabetic (*db/db*) mice. PV-OCT captures the structure of the vasculature network by detecting the dynamic changes in optical phase due to blood flow [18, 19], while FLIM tracks the metabolic activity in cells by probing the intrinsic fluorescence lifetime of intracellular reduced nicotinamide adenine dinucleotide (NADH) [20–22]. NADH is a coenzyme involved in a reduction-oxidation (redox) reaction, which can exist in 2 different states: free in the cytoplasm or bound to certain enzymes. By tracking the fluorescence lifetime of NADH at these 2 different states, the metabolic activity in the wounded skin can be analyzed [22]. These label-free, cellular-level resolution imaging techniques, together with the processing methods described here for in vivo longitudinal monitoring of wound healing, offer the potential to provide a more quantitative way to characterize the healing mechanisms of novel interventions and treatments. Most importantly, these noninvasive techniques provide direct assessment for determination of individual patient responses to emerging pharmacologic therapies.

2 | MATERIALS AND METHODS

2.1 | Experimental design

All animal procedures were performed under a protocol approved by the Institutional Animal Care and Use Committee at the University of Illinois at Urbana-Champaign. Male BKS.Cg-Dock7m +/+ Leprdb/J (*db/db*) diabetic mice (Jackson Laboratory, Harbor, Maine) were used in this study. The ear skin was chosen as a wounding site since it was less affected by breathing motion, and readily allowed for the observation of microvascular regeneration and the effect of the topical cream. Ear skin preparation and wounding were performed under anesthesia (1.5% isofluorane gas mixed with 2% oxygen) using a surgical microscope. Hair on the right ear skin was removed with surgical tweezers to reduce possible autofluorescent signals from the skin hair. The skin was then cleaned with rubbing alcohol, and a full thickness excisional wound, which included the entire layer of skin on top of the cartilage of the ear, was made using a sterile 1-mm-biopsy punch (Miltex Inc., Miami, Florida). It is important to note that the ears were not pierced completely through during the wounding process. The skin was then gently cleaned again with rubbing alcohol.

Two groups of animals, treated and placebo, were involved in this study, and both the angiogenesis-promoting topical formulation and the placebo (drug vehicle only), were prepared and provided by GlaxoSmithKline. The treatment group (*n* = 5) received daily application of the angiogenesis-promoting ointment for 14 days, and the placebo group (*n* = 5) received daily application of the placebo vehicle for 14 days. On day 0 of the study, both multimodal microscope images and digital photographs of nonwounded skin from all animals were acquired. All animals were wounded on day 1, followed by microscopy imaging and digital photographing, and then the respective treatments were applied to the wounds of the designated animal group. Longitudinal in vivo multimodal imaging of the wounds from both groups was performed under anesthesia on days 1, 3, 7, 10, 14, 21, and 28. On all imaging days, the mouse ear was carefully mounted to minimize the amount of motion artifact due to breathing, which can greatly affect

the quality of the vascular imaging. During the treatment period (days 1-14), the treatments were applied each day after imaging and photographing. The wounds were left uncovered, and no analgesics or additional agents were administered to the mice during the course of the study.

2.2 | Multimodal microscopy

Imaging of the skin was performed using a custom-built integrated PV-OCT and FLIM microscope system (Figure 1) [23–25]. The capability to perform both OCT and FLIM imaging in one system without the need to move the animal provides both the structural information of the microvasculature network and the functional information of the cellular metabolic activity, respectively, during wound healing from the same regions of interest on the skin. The system uses a tunable titanium: sapphire laser (Mai Tai HP; Spectra Physics, Santa Clara, CA) as the source, and the center wavelengths of excitation were 800 nm for PV-OCT and 730 nm for FLIM. The spectral-domain OCT system was based on a free-space Michelson interferometer with a spectrometer in the detection arm. The OCT axial and transverse resolutions were 5 and 25 μm, respectively. FLIM signals were detected by a 16-channel photomultiplier tube spectrometer (PML-16-C; Becker-Hickl, Berlin, Germany) and captured with a time-correlated single photon counting data acquisition board (SPC-150; Becker-Hickl). The maximal intensity projection images of the volumetric PV-OCT dataset were constructed during post processing utilizing MATLAB (Mathworks, Natick, MA), and fluorescence lifetime curves were obtained using the associated commercial software (SPCImage; Becker-Hickl) as per Section 2.3. To switch from OCT to FLIM imaging, a change of objective was needed, which was done in less than a minute without moving the animal.
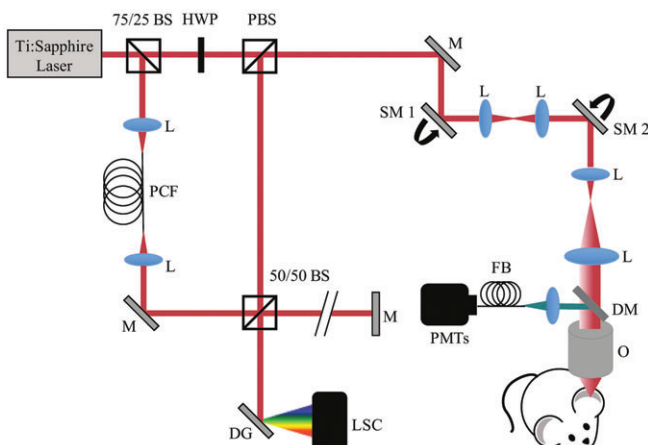
FIGURE 1 Schematic of the multimodal microscope system. BS, Beam splitter; HWP, half-wave plate; L, lens; PCF, photonic crystal fiber; PBS, polarized beam splitter; M, mirror; SM, scanning mirror; DM, dichroic mirror; FB, fiber bundle; DG, diffractive grating; LSC, line scan camera

2.3 | Image analysis

All vessel analyses from the PV-OCT images were performed utilizing MATLAB. Three different parameters were quantified to evaluate the angiogenesis-promoting effect of the active agent: overall vessel density, vessel branching point density and mean vessel diameter. The rationale for choosing these 3 parameters is discussed in the Section 3. PV-OCT images were first processed using contrast-limited adaptive histogram equalization in MATLAB to enhance contrast, and then filtered using a medium filter. The filtered images were then segmented using Otsu's method to obtain binary images of the vessel structures for all subsequent analyses.

To determine the overall vessel density, the total number of segmented vessel pixels in the binary images was divided by the total image area (in pixels), excluding the signal-free wound area. Vessel branching points were calculated by first skeletonizing the binarized vessel image, and then identifying all the vessel connecting points. Following this, the number of connecting points was divided by the total image area, excluding the signal-free wound area. To determine the mean vessel diameter, the binary image of the vessels was first skeletonized to identify the midline of each vessel. The distances between the midline and the vessel boundary (radius) at all points were then calculated, and the vessel diameters at all locations were obtained by multiplying these acquired radii by 2. The mean vessel diameter across the entire image was then calculated by dividing the sum of the vessel diameters from all locations by the number of identified vessel diameters.

FLIM analysis was performed using SPCImage software (Becker-Hickl). The biexponential fluorescence decay model was fit to the recorded dataset at each pixel to acquire the 4 parameters used for comparison in this study: mean fluorescence lifetime, relative ratio of protein-bound NADH to free NADH, fluorescence lifetime of protein-bound NADH and fluorescence lifetime of free NADH. In addition, the χ^2 value at each pixel, which indicates the goodness of fit of the fluorescence decay curve at each pixel, was used to identify the pixels with poor fits to the decay curve. The data from these pixels were then discarded and not included in the analysis.

2.4 | Statistical analysis

All data are represented as means $\pm$ SE. Two-way repeated measures ANOVA (8 × 2) were used to investigate main and combined effects of time and treatment, followed by Fisher's least significant difference post hoc analysis. Statistical analysis was performed using MATLAB, and differences were considered significant at $p \leq 0.05$.

3 | RESULTS

3.1 | Regeneration of the microvasculature network

In this study, the ear skin was chosen as a wound model due to the ease of access to the microvascular network,

which is necessary for fulfilling the goal of the study. During each imaging session, the mouse ear was carefully positioned to ensure the entire wound was within the field-of-view during scanning. Figure 2A illustrates the PV-OCT images of both treatment and placebo groups on selected days to show the changes in the microvasculature network during healing. It should be noted that due to the relatively thin skin on the mouse ear and impractical wound coverage options, the ear wounds on all mice became full-thickness holes after approximately 1 week. However, this was consistent across all animals, and the morphological changes in the wounded skin could still be monitored. Visual comparison between the 2 groups shows a noticeably denser vessel network around the edges of the healing wounds in the treated group, compared to the placebo group (Figure 2A).

To confirm this visual observation, overall vessel density was calculated, as described in Section 2.3. The results in Figure 2B show that the overall vessel density in the treatment group was significantly higher ($p \leq 0.05$) than in the placebo group during treatment. During the early stages of wound healing, the angiogenesis process produces additional microvessels to increase the efficiency of oxygen and nutrient delivery, and to sustain newly formed tissue. This process usually ceases after the reepithelialization and granulation tissue formation stage, which often lasts for approximately 10 days [5].

To investigate whether the increase in overall vessel density observed previously was caused by an increase in angiogenesis or an enlargement of vessel diameters, both the vessel branching point density and the average vessel diameter parameters were calculated. Results show that the treatment group experienced an increase in branching point density in the first week after wounding, which was significantly higher than the placebo group (Figure 2C). This suggests that the treatment group experienced an increase in angiogenesis during the early stage of wound healing. In contrast, the placebo group shows a gradual decrease in branching point density after wounding. In addition, further investigation of the volumetric PV-OCT dataset shows a noticeable increase in the amount of small vessels in the superficial layers of the skin in the treatment group, which overshadows some of the larger vessels that are visible in days 1 and 7 but not in later days (Figure 2A). Figure S1 (Supporting Information) illustrates the presence of these
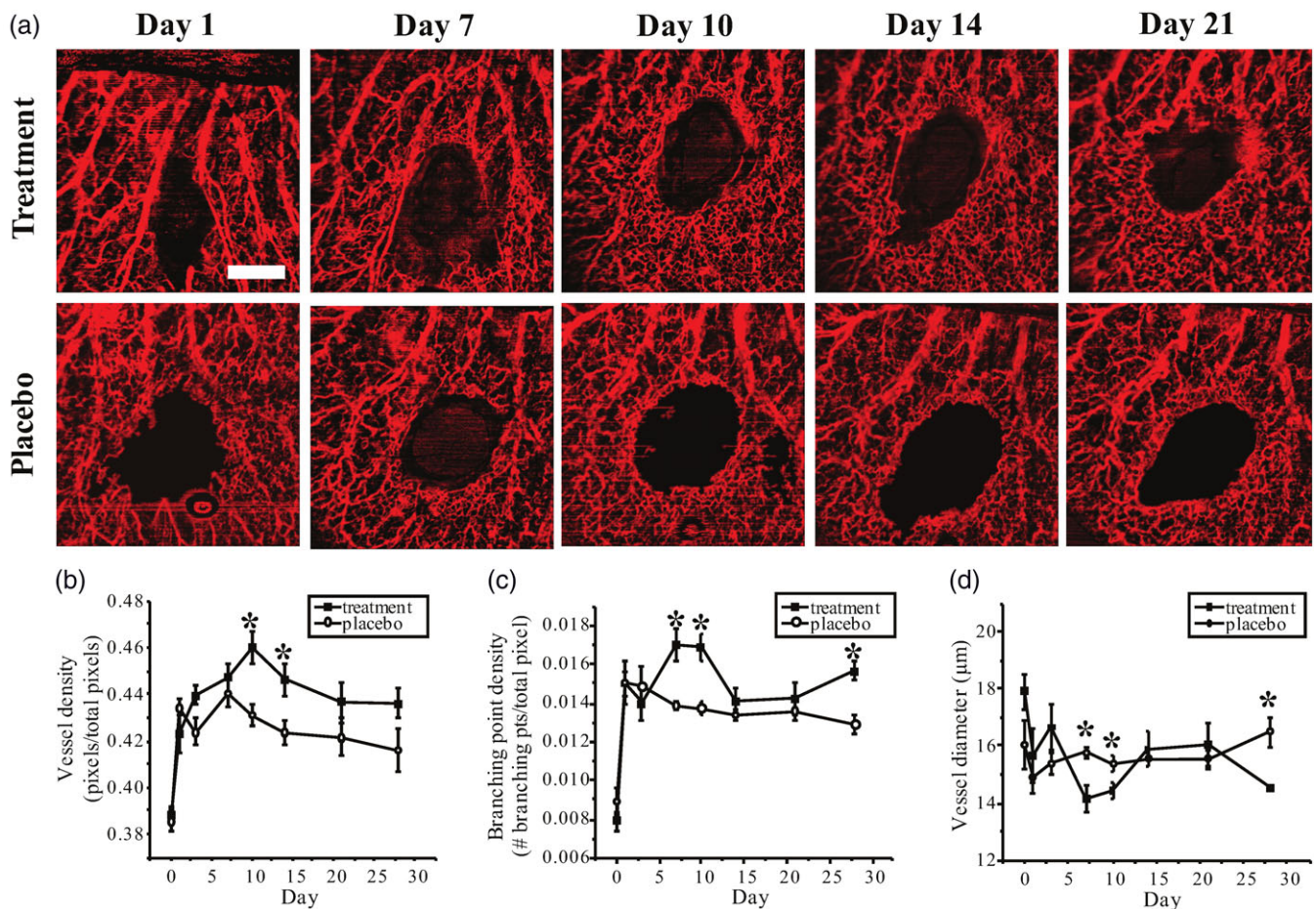
FIGURE 2   PV-OCT and vessel analysis show that the treatment group experienced a higher level of angiogenesis during wound healing. (A) PV-OCT images of both treatment and placebo groups. (B) Analysis shows a significantly higher vessel density in the treatment group. (C) Treatment group has a significant increase in branching point density. (D) Treatment group experienced a decrease in vessel diameter. *Treatment group has significantly higher/lower values than placebo group ($p \leq 0.05$). Scale bar: 500 μm applies to all

larger vessels in the deeper layers of the volumetric dataset.

To quantify the change in vessel diameters during the study period, the mean vessel diameter on each day was calculated, as shown in Figure 2D. Both groups show some variation in diameter during the healing process. However, only the treatment group shows a notable decrease in mean diameter during the first week of healing, which is significantly lower than the placebo group during treatment. This decrease in mean vessel diameter and increase in branching point density in the treatment group could suggest an increase in the number of smaller vessels, which is expected during the early stage of angiogenesis [26]. Comparison across these parameters suggests a correlation between the increase in vessel density and the increase in vessel branching in the treated group.

3.2 | Identification of hypoxia in keratinocytes

The area of the skin surrounding each wound was imaged using FLIM each imaging day to assess the effect of the topical cream on the cellular metabolic activity in the skin. For each animal, after the OCT vasculature image was acquired, regions around the wound bed were selected for FLIM imaging (Figure S2). Representative FLIM images of both treatment and placebo groups are shown in Figure 3A, and a color scale representing the fluorescence lifetime

range is included. Clear visual differences can be seen in the FLIM images between the 2 groups. It is evident from the FLIM images that the treatment group has a larger representation of lower lifetime components (red hues) during the treatment period (Figure 3A) than do the controls.

The mean NADH fluorescence lifetime was calculated from the corresponding fit parameters using Eq. (1), where τ_m is the mean NADH lifetime, a_1 and a_2 are the relative concentrations of free NADH and protein-bound NADH, respectively, and τ_1 and τ_2 are the excited state lifetimes of free NADH and protein-bound NADH, respectively [14, 25, 27].

$$\tau_m = a_1\tau_1 + a_2\tau_2. \tag{1}$$

Results show that the treatment group has a shorter lifetime during the course of topical application (days 1-14), while the placebo group experienced an increase in mean lifetime during healing (τ_m, Figure 3B), which has been previously observed in wounded skin [12, 28]. In addition, statistical analysis shows that the mean lifetime in the treatment group was significantly lower ($p \leq 0.05$) than the placebo group during treatment period. A decrease in mean fluorescence lifetime is usually caused by the presence of more short lifetime components (free NADH) than long lifetime components (protein-bound NADH), which suggests a metabolic shift from oxidative phosphorylation toward
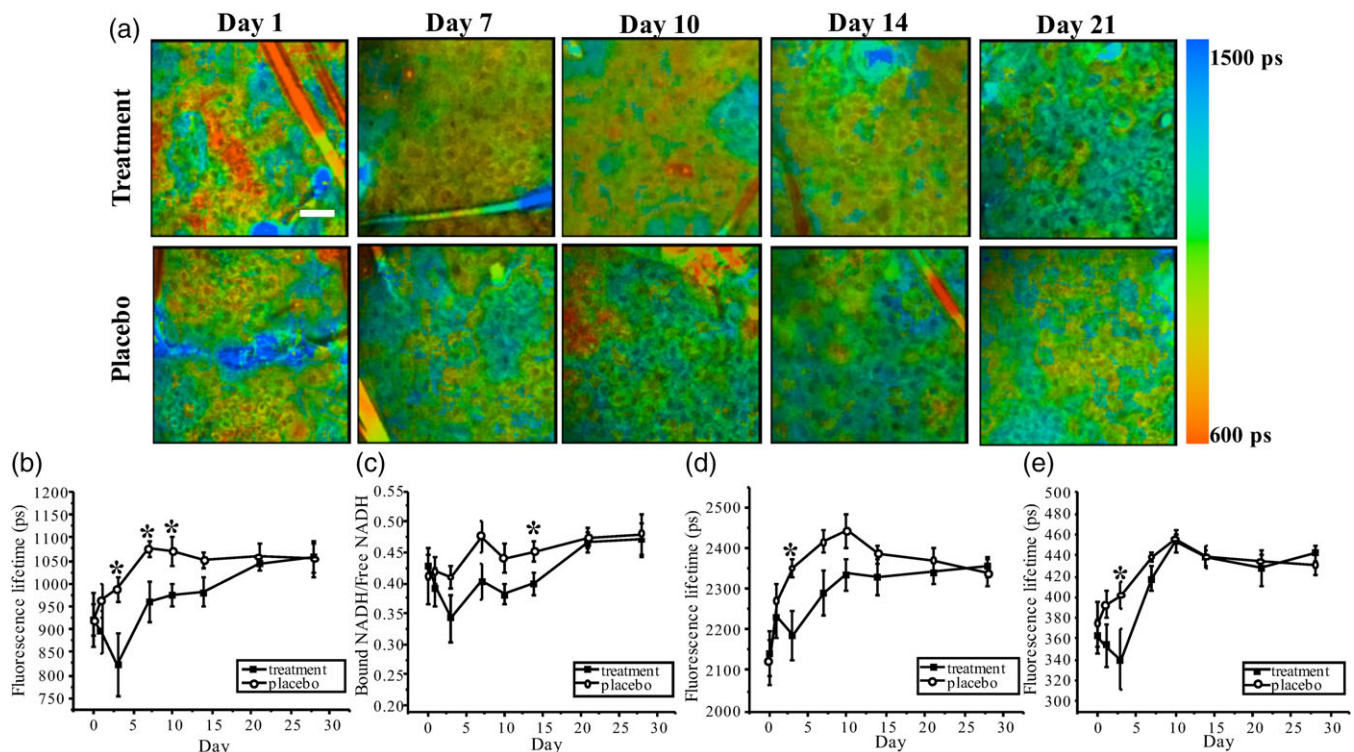
FIGURE 3 FLIM analysis shows that the treatment group experienced a hypoxic reaction during the drug application period. (A) FLIM images of the treatment group have more red hues during the treatment period. (B) The mean NADH fluorescence lifetime in the treatment group is significantly shorter than in the placebo group. (C) Ratio of protein-bound and free NADH is also significantly lower in the treated mice. (D) Treatment group has significantly shorter protein-bound NADH excited state lifetimes. (E) Treatment group shows significantly shorter free NADH excited state lifetimes on day 3.
*Treatment group has significantly smaller values than placebo group ($p \leq 0.05$). Scale bar: 20 μm applies to all

glycolysis [22]. To further investigate the cause of the decreased mean NADH lifetime in the treatment group, additional parameters were calculated. The ratio of protein-bound NADH and free NADH components (a_2/a_1) was calculated each day to examine changes in the relative concentrations of the 2 components. Figure 3C shows that the bound-to-free NADH ratio in the treatment group is significantly lower than in the placebo group, suggesting that there is an increased level of glycolysis, which is often observed under hypoxic condition and supports an HIF induction related switch to glycolytic mechanisms consistent with prolyl hydroxylase inhibition [7, 22, 29].

In addition, differences between the treatment and placebo groups during the treatment period were also found between bound (τ_2) and free (τ_1) NADH lifetimes, as illustrated in Figure 3D,E. The treatment group has a significantly lower bound NADH lifetime than placebo on certain days (Figure 3D), which can be explained by NADH binding to shorter lifetime enzymes or proteins, causing the bound NADH lifetime to decrease [29]. The free NADH lifetimes in both groups have similar trends throughout the study, except for a decrease in the treatment group on day 3, which has also been previously observed under hypoxic condition [22]. This analysis shows that the decrease in mean NADH lifetime in Figure 3D is caused by the decreases in the bound-to-free NADH ratio, the bound NADH lifetime and the free NADH lifetime. All of these observations suggest that there is an increase in glycolysis in the wounded skin treated with the active agent, which is consistent with a hypoxic environment [22, 29].

4 | DISCUSSION

This study presents an in vivo, label-free cellular-level approach to quantitatively characterize the microvascular and metabolic skin wound healing mechanisms of an angiogenesis promoting, as well as metabolic shifting, topical treatment that mimics the hypoxic environment through inhibition of prolyl hydroxylase. PV-OCT imaging and analysis show that the ear wounds in mice treated with this angiogenesis-promoting agent demonstrate a significant increase in vessel density. Analysis of vessel branching and diameter further suggests that this increase in vessel density is due to vessel branching and production of additional microvessels in order to support the increased demand for oxygen and nutrients in wounded skin during the initial time period of healing [5, 30]. The decrease in vessel branching and increase in vessel diameter after the first 2 weeks could be associated with the cessation of the treatment application, or the disintegration of these newly formed blood vessels through apoptosis as demand for additional nutrient support during rebuilding is no longer necessary [5]. Additional studies will be necessary to further investigate the cause(s) of these changes.

FLIM illustrates a significant decrease in the mean NADH fluorescence lifetime (τ_m) in the treatment group shortly before and during the same period of time as when a significant increase in vessel density was observed. Analysis of the FLIM parameters also revealed significant decreases in bound-to-free NADH ratio (a_2/a_1) and the lifetime of protein-bound NADH (τ_2). In addition, the lifetime of free NADH (τ_1) also exhibits a slight decrease during the treatment. These results suggest that the primary mechanisms responsible for the significantly lower mean NADH lifetime is the relative decrease in the amount of protein-bound NADH and the bound NADH lifetime, which is likely due to NADH binding to shorter lifetime enzymes [22]. These observations further suggest that there is an increase in glycolysis in the treatment group during the period of topical application, since cells favor glycolysis over oxidative phosphorylation for ATP production under hypoxic conditions, and consistent with induction of HIF via inhibition of prolyl hydroxylase [22, 29, 31]. Furthermore, significant changes in fluorescence lifetimes occur shortly before and while significant differences in PV-OCT parameters are detected, suggesting that the chemical environment of cells reacts to the treatment prior to the physiological changes in the skin. This can be further understood by considering that the angiogenesis process usually begins after sensing a change in the metabolic environment, and after receiving proper chemical signals from various cytokines and angiogenic factors [6, 32].

With the expected rise of diabetes in the general population, an active area of research has been in developing treatment strategies for nonhealing diabetic wounds. Understanding the healing mechanisms of novel treatments is also an essential part of drug and therapy development. In this study, we demonstrate a label-free and more direct way to observe and quantify microvascular and metabolic healing mechanisms, and the biological response to a topical treatment, utilizing a multimodal microscope equipped with OCT and FLIM. This advancement is relevant due to the limited ability to assess wound physiology or treatment effects in patients with chronic wounds or delayed healing. While additional studies are required to further understand the larger number of complex healing mechanisms involved in the skin wound healing process, the cross-modality correlation between PV-OCT and FLIM presented here successfully relates the increase in vasculature density to the relative changes in cellular metabolism in living animals.

Future studies will investigate if differences exist in wound healing closure rates between different skin sites, such as for wounds on the dorsal skin or the limbs, as well as for larger wound sizes. Also, additional characterization parameters may be included, such as dynamic scattering contrast, to potentially probe the intracellular motion including mitochondria activities and other ATP-consuming motion [33, 34]. Together, these preliminary in vivo results suggest that this topical treatment is capable of promoting

angiogenesis and increase glycolysis in wounded diabetic skin by mimicking hypoxia in the surrounding cellular environment consistent with HIF mechanisms. Most importantly, the use of this multimodal optical imaging approach, combined with quantitative image analysis, can follow the morphologic, microvascular and metabolic changes in the wound healing process in ways not possible with many current evaluation methods. The insights demonstrated in this study could lead to new noninvasive endpoints for evaluation of the efficacy of new therapeutics in environments that do not permit traditional assessments, and lead to more direct ways of detecting personalized patient responses to treatment.

AUTHOR BIOGRAPHIES

Please see Supporting Information online.

REFERENCES

[1] American Diabetes Association. Diabetes statistics, http://www.diabetes.org/ (accessed: October 2016).

[2] Centers for Disease Control and Prevention. National diabetes statistics report, 2014, http://www.cdc.gov/diabetes/data/statistics/2014statisticsreport.html (accessed: October 2016).

[3] B. D. Pence, J. A. Woods, *Adv. Wound Care* 2014, *3*, 71.

[4] H. Brem, M. Tomic-Canic, *J. Clin. Invest.*, 2007, *117*, 1219.

[5] A. J. Singer, R. A. Clark, *N. Engl. J. Med.* 1999, *341*, 738.

[6] P. Martin, *Science* 1997, *276*(5309), 75.

[7] I. R. Botusan, V. G. Sunkari, O. Savu, A. I. Catrina, J. Grünler, S. Lindberg, T. Pereira, S. Ylä-Herttuala, L. Poellinger, K. Brismar, S.-B. Catrina, *Proc. Natl. Acad. Sci. U.S.A.* 2008, *105*, 19426.

[8] Y. Wu, L. Chen, P. G. Scott, E. E. Tredget, *Stem Cells* 2007, *25*, 2648.

[9] R. D. Galiano, O. M. Tepper, C. R. Pelo, K. A. Bhatt, M. Callaghan, N. Bastidas, S. Bunting, H. G. Steinmetz, G. C. Gurtner, *Am. J. Pathol.* 2004, *164*, 1935.

[10] M. Galeano, D. Altavilla, D. Cucinotta, G. T. Russo, M. Calò, A. Bitto, H. Marini, R. Marini, E. B. Adamo, P. Seminara, L. Minutoli, V. Torre, F. Squadrito, *Diabetes* 2004, *53*, 2509.

[11] C. W. Pugh, P. J. Ratcliffe, *Nat. Med.* 2003, *9*, 677.

[12] J. Li, A. J. Bower, V. Vainstein, Z. Gluzman-Poltorak, E. J. Chaney, M. Marjanovic, L. A. Basile, S. A. Boppart, *Biomed. Opt. Express* 2015, *6*, 4277.

[13] J. Li, Y. Pincu, M. Marjanovic, A. J. Bower, E. J. Chaney, T. Jensen, M. D. Boppart, S. A. Boppart, *J. Biomed. Opt.* 2016, *21*, 086006.

[14] A. J. Bower, M. Marjanovic, Y. Zhao, J. Li, E. J. Chaney, S. A. Boppart, *J. Biophotonics* 2017, *10*, 143. https://doi.org/10.1002/jbio.201600003.

[15] H. Tu, Y. Liu, D. Turchinovich, M. Marjanovic, J. K. Lyngsø, J. Lægsgaard, E. J. Chaney, Y. Zhao, S. You, W. L. Wilson, B. Xu, M. Dantus, S. A. Boppart, *Nat. Photonics* 2016, *10*, 534.

[16] M. Balu, K. M. Kelly, C. B. Zachary, R. M. Harris, T. B. Krasieva, K. Konig, A. J. Durkin, B. J. Tromberg, *Cancer Res.* 2014, *74*, 2688.

[17] L. H. Laiho, S. Pelet, T. M. Hancewicz, P. D. Kaplan, P. T. C. So, *J. Biomed. Opt.* 2005, *10*, 024016.

[18] B. J. Vakoc, R. M. Lanning, J. A. Tyrrell, T. P. Padera, L. A. Bartlett, T. Stylianopoulos, L. L. Munn, G. J. Tearney, D. Fukumura, R. K. Jain, B. E. Bouma, *Nat. Med.* 2009, *15*, 1219.

[19] L. An, J. Qin, R. K. Wang, *Opt. Express* 2010, *18*, 8220.

[20] M. Balu, A. Mazhar, C. K. Hayakawa, R. Mittal, T. B. Krasieva, K. Konig, V. Venugopalan, B. J. Tromberg, *Biophys. J.* 2013, *104*, 258.

[21] J. R. Lakowicz, H. Szmacinski, K. Nowaczyk, M. L. Johnson, *Proc. Natl. Acad. Sci. U.S.A.* 1992, *89*, 1271.

[22] M. C. Skala, K. M. Riching, A. Gendron-Fitzpatrick, J. Eickhoff, K. W. Eliceiri, J. G. White, N. Ramanujam, *Proc. Natl. Acad. Sci. U.S.A.* 2007, *104*, 19494.

[23] B. W. Graf, A. J. Bower, E. J. Chaney, M. Marjanovic, S. G. Adie, M. De Lisio, M. C. Valero, M. D. Boppart, S. A. Boppart, *J. Biophotonics* 2014, *7*, 96.

[24] B. W. Graf, E. J. Chaney, M. Marjanovic, S. G. Adie, M. De Lisio, M. C. Valero, M. D. Boppart, S. A. Boppart, *Technology* 2013, *01*, 8.

[25] Y. Zhao, M. Marjanovic, E. J. Chaney, B. W. Graf, Z. Mahmassani, M. D. Boppart, S. A. Boppart, *Biomed. Opt. Express* 2014, *5*, 3699.

[26] P. Carmeliet, *Nat. Med.* 2003, *9*, 653.

[27] H. G. Breunig, H. Studier, K. Konig, *Opt. Express* 2010, *18*, 7857.

[28] M. J. Im, J. E. Hoopes, *J. Surg. Res.* 1970, *10*, 459.

[29] D. K. Bird, L. Yan, K. M. Vrotsos, K. W. Eliceiri, E. M. Vaughan, P. J. Keely, J. G. White, N. Ramanujam, *Cancer Res.* 2005, *65*, 8766.

[30] V. Falanga, *Lancet* 2005, *366*, 1736.

[31] M. G. Vander Heiden, L. C. Cantley, C. B. Thompson, *Science* 2009, *324*, 1029.

[32] J. Folkman, *Nat. Med.* 1995, *1*, 27.

[33] C. Apelian, F. Harms, O. Thouvenin, A. C. Boccara, *Biomed. Opt. Express* 2016, *7*, 1511.

[34] G. Farhat, A. Mariampillai, V. X. D. Yang, G. J. Czarnota, M. C. Kolios, *J. Biomed. Opt.* 2011, *16*, 070505.

SUPPORTING INFORMATION

Additional Supporting Information may be found online in the supporting information tab for this article.

Figure S1. PV-OCT images illustrating the presence of larger vessels in deeper layers of the skin (circled in yellow). Comparison with Figure 2 shows that these are the same large vessels observed in days 1 and 7 in the treatment group. Scale bar: 500 μm applies to all

Figure S2. Composite image of skin structure and vasculature OCT with selected regions of FLIM imaging